Research Square

Preprints are preliminary reports that have not undergone peer review.
They should not be considered conclusive, used to inform clinical practice,
or referenced by the media as validated information.

Microglia-to-Neuron Mitochondrial Transfer Supports Neuronal Metabolism and Protects Against Neurodegeneration

Monara Kaelle Servulo Cruz Angelim
State University of Campinas
Lincon Felipe Lima Silva
State University of Campinas
Gisele Castro
State University of Campinas
Wilias Silva Santos Greison
State University of Campinas
Rodrigo Dias Requião
State University of Campinas
Guilherme Augusto da Silva Nogueira
State University of Campinas
Thiago Pereira Campos
Universidade Federal do Ceará
Celia Bresil
State University of Campinas
Mariana Ozello Baratti
State University of Campinas
Webster Leonardo Guimarães da Costa
State University of Campinas
Matheus Barbosa
State University of Campinas
Francisco Breno Silva Teofilo
State University of Campinas
Hernandes F Carvalho
State University of Campinas
Licio A Velloso
State University of Campinas
Pedro M Moraes Vieira
pmvieira@unicamp.br

State University of Campinas

Research Article

Keywords: Microglia, Mitochondria transfer, Oxidative Metabolism, Neuroprotection, Oxidative stress, Parkinson's disease

Posted Date: May 13th, 2026

DOI: https://doi.org/10.21203/rs.3.rs-9558181/v1

License: This work is licensed under a Creative Commons Attribution 4.0 International License. Read Full License

Additional Declarations: No competing interests reported.

Abstract

Intercellular mitochondrial transfer is an emerging neuroprotective mechanism, yet the pathways governing microglial donation and the functional relevance of distinct extracellular mitochondrial forms remain unclear. Using microglia expressing fluorescently tagged mitochondria, we show that microglia release mitochondria upon direct contact with injured neurons, generating naked mitochondria and mitovesicles. Hypothalamic orexigenic neurons internalize these organelles, a process enhanced by mitochondrial stress. Transfer is contact-dependent, requires ROCK1/2 activity, is independent of exosome biogenesis, and is markedly reduced by neuronal Connexin 43 (Cx43) deficiency, identifying Cx43-enriched contact sites as hubs for mitochondrial acquisition. Functionally, transfer enhances neuronal survival after rotenone exposure and promotes oxidative respiration and nicotinamide nucleotide turnover. However, redox outcomes depend on donor state: mitochondria from naïve microglia reduce oxidative stress, whereas those from LPS-stimulated microglia exacerbate it. In vivo, microglial mitochondria are detected in hypothalamic and dopaminergic neurons, and exogenous delivery modulates feeding behavior and partially rescues rotenone-induced deficits in a Parkinsonian model.

Significance Statement

Neuroinflammation and mitochondrial dysfunction drive devastating brain disorders such as Parkinson's disease. This study reveals that microglia, the brain's immune cells, can transfer healthy mitochondria to stressed neurons through a specialized contact-dependent mechanism. This donation rescues neuronal metabolism, reduces oxidative damage, and preserves axonal integrity. However, the outcome depends critically on the microglial state since mitochondria from activated microglia can exacerbate injury. We demonstrate this process occurs naturally in the brain and can be harnessed therapeutically to improve motor function in a Parkinson's model. These findings uncover a fundamental immunometabolic communication pathway with broad implications for treating neurodegenerative and metabolic diseases.

Introduction

Mitochondria dysfunction is a central driver in neuroinflammatory and neurodegenerative diseases such as Parkinson’s and Alzheimer’s. While neurons rely on mitochondrial integrity, neuronal dysfunction is exacerbated by microglia, which can amplify oxidative stress metabolic imbalance and inflammation[1–3]. However, beyond their inflammatory role, microglia also exhibited protective functions, including the intercellular transfer of mitochondria[4,5], an emerging mechanism of metabolic support whose full significance for neuronal resilience is still being defined.

Emerging evidence indicates that stressed neurons can internalize functional mitochondria released by microglia to support bioenergetics and survival[4,6]. However, this process is double-edged as microglia can also release dysfunctional mitochondria, which propagate neurodegeneration by, for example, triggering pathogenic A1 astrocytic responses[5]. The switch between these protective and detrimental

outcomes is governed by a complex interplay of cellular metabolic state, cytoskeletal dynamics, and specific vesicular trafficking and uptake pathways[7,8]. Deciphering this regulatory network is therefore critical for developing therapeutic strategies that can selectively enhance beneficial mitochondrial transfer or correct metabolic impairments in neuroinflammatory diseases.

Critical knowledge gaps remain regarding whether microglial mitochondria transfer operates as a targeted rescue mechanism *in vivo*, and how its efficacy is influenced by metabolic or neurodegenerative stress. To address this, we tested the hypothesis that this process constitutes a regulated form of intercellular metabolic support. Here, we show that microglia release distinct populations of mitochondria, either as naked organelles or enclosed within membrane-bound vesicles, which are internalized by neurons. This transfer rescues neuronal survival by alleviating oxidative stress, restoring respiration, and modulating neuropeptide expression. Furthermore, using *in vivo* models of obesity and Parkinson's disease (PD), we demonstrate that this pathway preserves circuit function and prevents axonal degeneration. Together, our findings define a direct mechanism through which microglia support neuronal integrity via mitochondria donation, revealing a novel target for therapeutic intervention in neuroinflammatory and metabolic disorders.

Results

Microglia release mitochondria upon direct contact with injured neurons

To determine whether microglia can release mitochondria, we employed primary microglia from LysM-CrePhAM^{floxed} mice, in which mitochondria are labelled with the fluorescent protein Dendra2. In this model, Dendra2 is selectively expressed in the mitochondrial matrix[9] of lysozyme-expressing cells, which in the CNS are predominantly microglia (Fig. 1A). This provides specific, constitutive green fluorescence labelling of the microglial mitochondria network. In monoculture, microglia showed no spontaneous mitochondria release. However, when co-cultured with neuronal cells, including primary neurons or the neuronal cell lines Neuro2a and Clu189, we observed limited extracellular mitochondria release (**Supplementary Figure S1A)**. We selected the Clu189 cell line for subsequent studies due to its relevance to energy metabolism and its capacity for spontaneous neuronal differentiation without exogenous inducers **(Figure S1B**). Clu189 cells are derived from hypothalamic orexigenic neurons and express AgRP neuropeptide[10].

To assess the influence of neuronal injury on microglia mitochondrial release, we exposed Clu189 neurons to rotenone, a mitochondrial complex I inhibitor that induces oxidative stress and neuronal death[11,12]. Upon adding primary microglia to injured neuronal culture, time-lapse microscopy over 24 hours revealed that rotenone-induced injury triggered a marked increase in the release of Dendra2^{+} mitochondria from microglia. This suggests that damaged neurons emit signals which actively recruit microglial mitochondria support. High-resolution imaging reveals two distinct forms of released

mitochondria: (i) small, membrane-free naked mitochondria and (ii) larger mitovesicles, which are membrane encapsulated structures containing single or multiple mitochondria; or yet, interconnected organelles (Fig. 1B-C, **video S1C**).

This mitochondrial release was a rapid microglial response, detectable within 1 hour of contact with injured neurons and peaking by 6 hours, at which point the extracellular space was populated with abundant Dendra2^{+} structures of both types. To investigate whether mitochondrial release is a general property or phenotype-dependent, we treated microglia with diverse stimuli (Mdivi-1, a mitochondria fission inhibitor; LPS; palmitate; and IL-4). All conditions triggered the release of both mitochondrial forms (Fig. 1D-E), indicating that mitochondria release is a conserved microglial response. While the exact extrusion mechanism for mitochondria remains to be captured, their consistent presence and Dendra2 labelling confirm their microglial origin (Fig. 1F).

Orexigenic neurons internalize microglia-derived mitochondria

We next investigated whether neurons could internalize the mitochondria released by microglia. After 24 hours of co-culture, immunofluorescence revealed the presence of Dendra2 inside Clu189 neurons, confirming that neurons do uptake microglia-derived mitochondria (Fig. 2A). This uptake was not a passive process; live-cell imaging captured neurons actively recruiting extracellular mitochondria by extending membrane projections toward mitovesicles (**video S2C**). Importantly, neuronal injury amplified this process; thus, uptake was nearly threefold higher when neurons were pre-treated with rotenone, indicating that metabolic stress potently enhances the internalization of microglial mitochondria (Fig. 2B). Notably, this enhanced uptake was independent of upstream changes in microglial mitochondria dynamics, since promoting fission with LPS or palmitate and fusion with Mdivi-1 + M1 (**Figure S2A-B**) did not alter the overall capture of mitochondria (Fig. 2B). Functional analysis of the internalized mitochondria revealed a heterogenous population. While some Dendra2^{+} mitochondria retained membrane potential, as confirmed by co-localization with MitoTracker Deep Red, indicating they were metabolically competent upon entry (Fig. 2C), others do not retain membrane potential (Fig. 2D).

To define the mechanisms underlying mitochondrial transfer, we first probed the role of canonical vesicle trafficking in microglia. Inhibition of cytoskeleton-dependent pathways in microglia with the ROCK1/2 inhibitor Y27632 reduced neuronal mitochondrial uptake. In contrast, blocking exosome release via the N-SMase inhibitor GW4869 had no effect (Fig. 2E), suggesting that mitochondria are not conveyed through conventional exosomes. We next used a targeted CRISPR-Cas9 screen in Clu189 neurons to identify specific molecular mediators (**Figure S2C**). Knockout of Gja1, encoding the gap-junction protein Connexin 43 (Cx43), reduced mitochondrial uptake (Fig. 2F**)**, implicating Cx43 as a critical facilitator. In contrast, deletion of genes involved in alternative transfer pathways, such as *Exoc1* (Sec3) for tunnelling nanotubes[13]; *Gm609* (ISEC1), a CD200 homolog that interacts with microglial CD200R[14]; or *Itgb1* (Integrin β1)[15], had modest or negligible effects. In addition, high-resolution imaging revealed mitochondrial transfer at specialized contact sites between neurons and microglia, which served as

hubs for the accumulation of mitochondria (Fig. 2G). These microglial hubs enriched in mitochondria, formed around neuronal projections, may represent the sites at which Cx43 assembles functional gap junctions, thereby enabling direct mitochondrial transference. Together, our findings delineate a non-canonical intercellular pathway in which microglia release mitochondria via cytoskeleton-driven but exosome-independent mechanism, and neurons internalize them predominantly through Cx43-dedicated intercellular contact sites, regardless of the donor mitochondrial dynamics.

Neuronal survival is promoted by microglial mitochondria through metabolic support and ROS mitigation

To assess the functional impact of mitochondria transfer, we began by examining neuronal survival. As expected, exposure to rotenone let to increased neuronal death (Fig. 3A). However, when neurons were co-cultured with microglia, this toxicity was significantly reduced. Notably, blocking mitochondria transfer by culturing microglia on 1 µm pore transwell inserts abolished the protective effect, demonstrating that direct cell-to-cell contact is essential for microglia to confer neuroprotection through mitochondrial transfer.

To determine whether microglial mitochondria alone can provide neuroprotection, we supplemented rotenone-injured neurons with purified microglial mitochondria (**Figure S3A**). Although neurons successfully internalized these organelles (**Figure S3B**), neuronal death was not significantly reduced, despite a consistent trend toward protection (Fig. 3B). This finding suggests that full efficacy may require additional microglial factors or the context of active cell-to-cell transfer.

To elucidate the metabolic mechanisms underlying neuronal protection, we assessed glycolytic and mitochondrial function in injured neurons supplemented with microglial mitochondria. Glycolysis remained unchanged following mitochondria transfer, regardless of the prior activation state of the microglia (**Figure S3C**). In contrast, mitochondrial respiration was enhanced by mitochondria derived from naïve or Mdivi-1 + M1-treated microglia, but not by those from LPS-activated microglia (Fig. 3C). This increase in respiratory capacity was accompanied by accelerated NAD+/NAD(P)H turnover, directly reflecting improved mitochondrial activity (Fig. 3D).

Given that rotenone induces oxidative stress, we next examined the effect of extracellular mitochondria on neuronal ROS levels. Co-culture with naïve microglia effectively attenuated rotenone-induced ROS accumulation, whereas LPS-activated microglia exacerbated it (Fig. 3E).

This effect was intrinsic to the transferred mitochondria: supplementation with mitochondria purified from naïve microglia reduced neuronal ROS, while mitochondria from LPS- or Mdivi-1 + M1-treated microglia had no effect (Fig. 3F). Importantly, this reduction in ROS occurred without altering the mitochondrial membrane potential of neurons (Fig. 3G), indicating that the antioxidant effect was not due to mitochondrial depolarization. The therapeutic window for this antioxidant effect proved to be narrow and context-dependent: mitochondrial supplementation failed to protect undifferentiated

neuronal precursors (**Figure S3D**), and greater doses of isolated mitochondria increased oxidative stress (**Figure S3E**). These findings underscore the critical importance of both dosage and neuronal differentiation state in determining the efficacy of mitochondrial transfer.

Finally, we investigated whether mitochondrial uptake influenced the expression of neurotransmitters and the pro-inflammatory cytokine *Tnf*. Following rotenone injury, which increased both *AgRP* and *POMC* expression, transferred mitochondria selectively potentiated AgRP expression (**Figure S3F**). This was accompanied by induction of *Tnf* (**Figure S3G**), indicating that exogenous mitochondria can trigger coordinated transcriptional responses involving both metabolic (orexigenic) and inflammatory pathways. Collectively, these data reveal a tripartite mechanism of microglia-mediated support: transferred mitochondria rescue neuronal bioenergetics by enhancing oxidative respiration, mitigate cytotoxicity by limiting ROS accumulation, and remodel neuronal phenotype by modulating neuropeptide and inflammatory gene expression. This multifaceted intervention highlights the complexity of intercellular metabolic support in the injured brain.

Mitochondrial transfer occurs in the hypothalamus in vivo

To determine whether microglia-to-neuron mitochondria transfer occurs *in vivo*, we analyzed whole sagittal brain sections from PhAM mice. Dendra2^{+} mitochondria were widely distributed across several brain regions, including the cortex, hippocampus, cerebellum, thalamus and hypothalamus (Fig. 4A). Remarkably, within the hypothalamus, we observed a pronounced accumulation of Dendra2 signal inside neuronal cell bodies, particularly in the ventromedial hypothalamus (VMH) (Fig. 4B**)** and arcuate nucleus (Fig. 4C). Characterization of recipient neurons revealed a specific cellular tropism: a subset of Dendra2^{+} neurons were identified as orexigenic, co-localizing with AgRP immunoreactivity (Fig. 4D**)**. In contrast, there was no evidence of mitochondrial transfer to anorexigenic POMC^{+} neurons or to astrocytes in this region (Fig. 4D, S4A). These findings demonstrate that microglial mitochondrial transfer to neurons occurs also *in vivo*, exhibiting both regional specificity and a selective preference for AgRP-expressing orexigenic neurons within the arcuate nucleus.

Given the central role of AgRP neurons in energy homeostasis, we next examined whether their acquisition of microglial mitochondria is regulated by nutritional status. Quantification of Dendra2^{+} mitochondria in hypothalamic neurons revealed similar levels in mice fed either a standard chow or a high-fat diet (**Figure S4B**), suggesting that basal mitochondria transfer to this neuronal population is maintained independently of nutritional state.

To assess whether microglial mitochondria can directly modulate feeding behavior, we injected purified mitochondria into the third ventricle of both lean and obese mice (Fig. 4E). Interestingly, the effect on feeding behavior was dependent on metabolic state since in lean mice, mitochondria supplementation stimulated food intake, whereas in obese mice, it suppressed feeding (Fig. 4F). This bidirectional modulation indicates that transferred mitochondria influence central feeding circuits in a state-specific manner, integrating into and altering the activity of these neural pathways.

Therapeutic mitochondrial supplementation prevents axonal loss in Parkinson's disease model

Within the substantia nigra, we observed robust transfer of Dendra2$^+$ mitochondria to tyrosine hydroxylase-positive (TH$^+$) dopaminergic neurons (Fig. 5A, **inset "a"**). Building on this anatomical evidence of mitochondrial transfer to a vulnerable neuronal population, we directly tested the therapeutic potential of this process in a PD model. Motor deficits were induced in mice through systemic, chronic rotenone treatment until animals exhibited at least 50% reduction in baseline motor performance. Following a 24-hour washout period, mitochondria isolated from microglia were unilaterally injected into the substantia nigra *pars compacta* (SNpc) (Fig. 5B). The exogenous mitochondria were selectively internalized by ipsilateral SNpc TH$^+$ dopaminergic neurons with no detectable uptake in the contralateral hemisphere, conforming targeted local delivery (Fig. 5C). Intranigral mitochondrial therapy resulted in a partial but significant restoration of locomotor performance (Fig. 5D). Importantly, this structural and functional rescue was selective, as mitochondrial transfer did not alter rearing behavior (Fig. 5E), suggesting a compartmentalized therapeutic effect. Consistent with this interpretation, mitochondrial transfer significantly increased the density of TH$^+$ axonal projections to the thalamus (Fig. 5F) without affecting neuronal numbers (Fig. 5G), indicating that the functional improvement was causally linked to the preservation of dopaminergic axonal integrity rather than to global changes in motor output. Collectively, these findings establish microglial mitochondrial donation as a fundamental neuroprotective mechanism that preserves axonal integrity and motor activity in a PD model. By demonstrating that this pathway can be leveraged therapeutically, we reveal a targeted approach to reinforce neuronal metabolism at its most vulnerable point, the axon, offering a promising avenue to halt circuit-level failure in neurodegenerative diseases.

Discussion

Intercellular mitochondrial transfer has emerged as a key neuroprotective mechanism in the CNS. Here, we identify a previously unrecognized contact-dependent pathway by which microglia donate mitochondria to neurons following injury. This process involves rapid release of two mitochondrial populations, naked mitochondria and mitovesicles, through a ROCK1/2-dependent mechanism. We further demonstrate that neuronal Cx43-enriched contact sites serve as focal platforms for mitochondrial accumulation and uptake. Functionally, the impact of mitochondrial transfer depends on donor microglial state. Mitochondria from naïve microglia enhance neuronal oxidative phosphorylation, accelerate NAD(P)H turnover, reduce oxidative stress, and improve survival after rotenone injury. In contrast, mitochondria from LPS-activated microglia increase neuronal ROS, revealing a state-dependent duality. Importantly, *in vivo* evidence of microglial mitochondrial transfer to hypothalamic and nigral neurons confirms this as a physiological and adaptive response to stress.

Mechanistically, our data challenge the prevailing notion that mitochondrial fission is a prerequisite for extracellular release. Neither pharmacological promotion of fission nor fusion altered the process of

releasing mitochondria, indicating that microglia employ specialized export mechanisms that operate independently of the fission–fusion cycle. Supporting this, Joshi and collaborators[5] found that LPS stimulation altered mitochondrial morphology without changing release quantity, indicating that division is not the limiting factor. Instead, shifts in fission-fusion balance may predominantly dictate the functional quality, rather than the abundance of released mitochondria[16]. For instance, exposure to the metabolic stressor palmitate, which promotes mitochondrial fragmentation, does not reduce mitochondrial release. Instead, palmitate may enhance the functional integrity of released mitochondria, possibly through a lipid-driven shift on microglial oxidative metabolism[7].

Our findings demonstrated that neurons actively internalize mitochondria released from microglia, a process amplified by neuronal metabolic stress. This supports the emerging paradigm of mitochondria as dynamic transcellular communicators. Importantly, the uptake of organelles with preserved membrane potential represents a physiologically meaningful event that can rescue neuronal bioenergetics. Conversely, the transfer of depolarized or fragmented mitochondria may propagate inflammatory signaling[1,5]. Together, a fundamental duality appears, the same process can mediate neuroprotection or neurotoxicity depending on donor organelle integrity. Neuronal uptake of microglial mitochondria is mediated through Cx43-enriched contact sites. This extends the established role of Cx43 in astrocyte–neuron coupling to microglial communication[17–20], suggesting a broader model in which Cx43 organizes structural platforms for horizontal mitochondrial exchange. Cx43 has been implicated in several modes of mitochondria transfer, including Cx43-containing TNTs, Cx43 facilitates mitochondrial transfer through gap junctional Ca^{2+} signaling and the subsequent internalization of gap junctions into connexosomes, which carry whole mitochondria between neighboring cells[21–24]. Mitochondrial export is further supported by ROCK1/2-dependent vesicular trafficking and the formation of mitovesicles, a distinct class of mitochondrial-enriched extracellular structures[25,26]. Together with OPA1/SNX9-dependent mitochondria-derived vesicle pathways[27], these mechanisms likely coordinate mitochondrial quality control with selective intercellular delivery.

Transferred mitochondria also influence neuronal inflammatory signaling. Microglial mitochondria increased neuronal TNF-α expression, consistent with the presence of mitochondrial DAMPs such as mtDNA and mtROS within mitovesicles[28]. These signals may activate innate immune pathways and remodel neuronal metabolic programs, linking inflammatory signaling to bioenergetic adaptation[25].

Functionally, microglial mitochondria protect metabolically compromised neurons through dual mechanisms: restoration of oxidative phosphorylation and reduction of oxidative stress. This rescue is strictly donor dependent. While naïve microglial mitochondria enhance respiration and NAD(P)H turnover, likely strengthening antioxidant defenses, mitochondria from LPS-activated microglia fail to confer benefit and may exacerbate stress[5,16,29]. Importantly, transfer selectively augments oxidative metabolism without altering glycolysis, preserving neuronal metabolic identity. However, excessive mitochondrial supplementation overwhelms quality-control systems, highlighting a narrow therapeutic

window. Recipient differentiation state further influences efficacy, with mature oxidative neurons benefiting more than glycolytic precursors.

Our *in vivo* findings establish microglia-to-neuron mitochondrial transfer as an active process within physiologically relevant contexts of metabolic and neurodegenerative stress. In the hypothalamus, AgRP-expressing neurons internalize microglial mitochondria. Exogenous delivery of these organelles to lean mice amplified food intake, consistent with *in vitro* data showing increased AgRP expression, thereby positioning mitochondrial transfer as a metabolic amplifier for orexigenic neurons circuits[30]. This effect was state dependent, since in obese mice, mitochondria supplementation did not stimulate feeding. While the behavioral impact was clear, robust cellular internalization of exogeneous mitochondria was less pronounced than endogenous transfer, raising intriguing questions about the possible paracrine signaling factors controlling these events effects, particularly within key subregions like the VMH. Similarly, in SNpc, microglial mitochondria were found within dopaminergic neurons. Therapeutically, exogenous mitochondrial administration mitigated motor deficits and preserved axonal integrity in a rotenone-induced Parkinson's model. This demonstrates the potential of enhancing this endogenous pathway to support circuit resilience under neurodegenerative pressure[4].

Collectively, our findings reposition microglia-to-neuron mitochondrial transfer as a regulated, context-sensitive mechanism of brain homeostasis. The outcome, whether amplifying orexigenic drive, restoring metabolic sensitivity, or preserving axonal function, is determined by the interplay between the quality of donated mitochondria, the state of the donor microglia, and the pathophysiological context of the recipient tissue. This framework highlights both the therapeutic promise and complexity of targeting this pathway. Future studies should address whether full organelle functionality is required for neuroprotection or if specific molecular cargoes suffice, as well as the safety profile of mitochondrial interventions *in vivo*. Ultimately, our work reveals microglial mitochondrial donation as a sophisticated form of immunometabolic communication that shapes neural circuit function and systemic physiology.

Limitations and Future Directions

While this study defines a novel pathway for mitochondria transference and support, several limitations merit consideration. First, in our chronic rotenone model, the lack of significant dopaminergic cell body loss, potentially due to dosing or drug penetration, may have constrained the observable therapeutic window for mitochondrial rescue. Second, we did not evaluate the *in vivo* consequences of delivering dysfunctional mitochondria, a critical gap given our *in vitro* evidence that damaged mitochondria exacerbate neuroinflammation as also described. The functional ratio of released mitochondria is a key determinant of neuronal fate, highlighting the need to define the safety profile of mitochondrial interventions. Future studies should imply models with more pronounced neuronal loss and directly test the effects of mitochondria from activated microglia *in vivo* to translate this mechanism into a safe therapeutic strategy.

Materials and Methods

Animals

C57BL/6J (males, 8–10 weeks, 22–25 g) PhAM^{Floxed} and C57BL/6J LysM-Cre transgenic mice were obtained from The Jackson Laboratory and housed at the Multidisciplinary Center for Biological Research (CEMIB), Campinas University (UNICAMP, Brazil). The PhAM^{Floxed} mouse line expresses the photo-convertible fluorescent protein Dendra2, which is specifically localized to mitochondria. To selectively label mitochondria in myeloid cells, PhAM^{Floxed} mice were crossed with LysM-Cre mice, resulting in robust Dendra2 expression in myeloid-derived cells without altering mitochondrial morphology, as previously described[9]. Mice were maintained at 22 ± 1°C, 55 ± 5% humidity, 12-h light/dark cycle, with *ad libitum* access to food and water, and housed under specific pathogen-free conditions at the Animal Facility of the Institute of Biology, UNICAMP. Procedures were performed under anesthesia using a mixture of ketamine (100 mg/kg) and xylazine (10 mg/kg) applied intraperitoneally and euthanasia was achieved under deep anesthesia (5% isoflurane until no reflex) followed by cervical dislocation. All experimental procedures were carried out according to UNICAMP Animal Ethics Committee (protocol number 6301-1/2023). Unless otherwise stated, each experiment included at least 3 mice per group (when not specified), with 3 independent biological replicates and three technical replicates per assay.

Obesity

Obesity was induced by feeding mice a high-fat diet (Teklad TD93075; 55% kcal from fat) starting at six weeks of age for 12 weeks as previously described[31]. Age-matched controls received standard chow (Nuvilab® CR-1, Curitiba, Parana, Brazil; 4.9% kcal from fat). Body weight was recorded weekly throughout the feeding period.

Food Intake Assessment

Baseline food intake was measured daily for three consecutive days (D0–D3) prior to stereotaxic surgery (D5). Following surgery and recovery, mice were fasted for 24 hours on D9 with free access to water. Recombinant leptin (Sigma-Aldrich, Cat. #L4146) was then administered by intracerebroventricular injection into the third ventricle (10 µg in 2 µL), and food intake was recorded at 1, 3, 6, and 24 hours post-injection. In a separate cohort, mice were euthanized 30 minutes after leptin administration by anesthesia overdose, and the hypothalamus was rapidly dissected and collected for downstream protein analysis by western blotting.

Experimental Parkinson’s Disease Model

A Parkinson’s disease–like phenotype was induced by chronic intraperitoneal administration of rotenone, adapted from Cannon and collaborators[32]. Rotenone was prepared as a 50× stock solution in 100% DMSO and diluted in medium-chain triglyceride oil (98% MCT, 2% DMSO) to a final concentration of 3.0 mg/mL. Fresh solutions were prepared two to three times per week, protected from light, and vortexed before each injection. Rotenone was administered daily at a dose of 3 mg/kg (1 mL/kg injection

volume). Control animals received vehicle (MCT-DMSO) alone. All behavioral assessments were performed by an experimenter blinded to treatment conditions. Each experimental group consisted of 5 mice.

Behavioral Assessments

Mice were monitored weekly for the development of Parkinson-like symptoms using open-field and rearing tests. Animals were considered to display a Parkinsonian phenotype when both distance travelled and number of rears were reduced by more than 50% relative to baseline (D0). Open field test: mice were acclimated to the open-field apparatus (Activity Monitor IR EP149, Equipment Insight) for 1 hour per day on two consecutive days. All behavioral testing was conducted in a quiet, isolated room, free from external interruptions. Locomotor activity (total distance, velocity) was recorded for 3 minutes. Rearing test: Mice were trained for 2 days to minimize anxiety-related artifacts. Rearing behavior was assessed by placing each animal into a clear 1-L glass cylinder for 2 minutes while video recording. A rear was defined as elevation of the forelimbs above shoulder level with simultaneous contact of both forelimbs on the cylinder wall. Forelimb removal from the wall and return to the floor were required before a subsequent rear was counted[33]. The total number of rears per session was quantified for each animal.

Stereotaxic Brain Intervention

Mice were anesthetized and injected with tramadol (5 mg/kg) subcutaneously (*s.c.*). After loss of reflexes, animals were positioned in a stereotaxic apparatus, and the scalp was shaved and sterilized with an 1% iodine solution. Ophthalmic ointment was applied to prevent corneal drying. A midline incision was made to expose the skull. A stainless-steel guide cannula (26-gauge) was implanted into the lateral ventricle or the substantia nigra *pars compacta* according to the mouse brain atlas of Paxinos and Franklin[34]. For the lateral ventricle, the following coordinates relative to bregma were used: AP − 0.35 mm, ML − 1.0 mm, DV − 2.2 mm, as previously described[35]. For the substantia nigra, coordinates were AP − 3.0 mm, ML − 1.05 mm, DV − 4.7 mm. After surgery, mice were placed in a warmed recovery cage and continuously monitored until full consciousness. They were then returned to their home cages and observed daily for seven days for potential signs of infection or distress. Tramadol (5 mg/kg, *s.c.*) was administered once daily for two consecutive days to minimize postoperative discomfort. After the recovery period, mice were used for experimental procedures. All compounds and vehicles (sterile saline) were infused in a total volume of 1.0–2.0 µl for 1 min post-infusion to prevent reflux.

Mitochondria Isolation

Intact mitochondria were isolated using the Mitochondria/Cytosol Fractionation Kit (Abcam, Cat. #ab65320). Following isolation, mitochondrial protein content was quantified using the Pierce™ BCA Protein Assay Kit (Thermo Scientific, Cat. #23225) prior to all downstream applications, including stereotaxic injection. Mitochondrial integrity was validated by transmission electron microscopy. For *in vivo* delivery, 20 µg of mitochondrial protein was resuspended in 2 µL sterile PBS and injected

immediately after quantification, with mitochondria maintained on ice throughout the procedure. Control animals received an equivalent volume of vehicle.

Primary Microglia Culture

Primary microglia were isolated from P1-P5 LysM-CrePhAM^{floxed} neonates. Neonates' brains were mechanically dissociated in aseptic conditions and cultured in DMEM with 10% fetal bovine serum (FBS) and 1% penicillin-streptomycin (PS) to generate mixed glial cultures. Microglial proliferation was enhanced using L929-conditioned medium at a 1:3 ratio of DMEM. Astrocyte-conditioned medium was collected and filtered for subsequent use. Culture medium was replaced every other day until a confluent astrocytic monolayer with microglia growing on top was established. Microglia were harvested by shaking cultures at 37°C and 180 rpm for 1 hour. The microglia-containing supernatant was passed through a 70 µm cell strainer and centrifuged at 1,000 rpm for 5 minutes. Cells were counted and replated in DMEM supplemented with astrocyte-conditioned medium at a 1:3 ratio. For stimulation experiments, primary microglia were treated with lipopolysaccharide (LPS, strain O111:B4; Sigma-Aldrich, Cat. #L4391) at 100 ng/mL for 24 hours; sodium palmitate (Sigma-Aldrich, Cat. #P9767) at 200 µM or, when not specified, at 400 µM for 6 hours; Mdivi-1 (Cayman Chemical Company, Cat. #15559) at 50 µM for 1 hour; M1 (Sigma-Aldrich, Cat. #SML0629) at 10 µM for 1 hour; GW4869 (Sigma-Aldrich, Cat. #D1692) at 40 µM and Y27632 (Cayman Chemical Company, Cat. #10005583) at 10 µM for 1 hour.

Neuronal Cell Culture

Clu189, POMC, and Neuro2a neuronal cell lines were obtained from the American Type Culture Collection (ATCC) and maintained in DMEM supplemented with 10% FBS and 1% PS in a humidified incubator at 37°C with 5% CO_2. Cells were allowed to undergo spontaneous differentiation, after which they were reseeded for experimental assays. Neuronal injury was induced by treatment with rotenone (Sigma-Aldrich, Cat. #R8875) at 300 ng/mL for 6 hours or 100 ng/mL for 12 hours, as indicated.

Co-Culture Experiments

Following stimulation, microglial and neuronal cells were cocultured at a 1:1 ratio in the same well to allow direct cell–cell contact for 24 hours. Cellular interactions and mitochondrial transfer were assessed either by time-lapse microscopy over a 24-hour period or by flow cytometry, enabling quantitative and dynamic analysis of microglia–neuron communication. To assess neuronal mitochondrial uptake in the absence of direct mitochondrial transfer from microglia, coculture experiments were performed using transwell inserts with defined pore sizes. Primary Dendra2-expressing microglia were cocultured with Clu189 neurons using inserts with pore diameters of 0.2 µm or 3.0 µm, which respectively restrict or permit mitochondrial passage while preventing direct cell–cell contact. Microglial cells were seeded onto the transwell inserts and maintained in DMEM, then stimulated according to the experimental protocol. In parallel, Clu189 neurons were treated with rotenone (200 nM) for 6 hours. Following stimulation and washing steps, transwell inserts were placed into wells containing neurons. After 24 hours of coculture, cells were harvested and processed for downstream analyses.

Immunofluorescence

For tissue immunofluorescence, mice were transcardially perfused with 20 mL of 1× PBS followed by 20 mL of 4% paraformaldehyde (PFA). Brains were dissected, washed in PBS, cryoprotected overnight in 15% sucrose followed by 30% sucrose, embedded in OCT compound, and frozen on dry ice. Coronal or sagittal brain sections (20–40 µm thick) were obtained using a cryostat (Leica CM1950). Sections were permeabilized and blocked for 1 hour at room temperature (RT) in PBS containing 5% bovine serum albumin (BSA) and 0.2% Triton X-100. For NeuN immunostaining, antigen retrieval was performed prior to blocking by incubating sections in citrate buffer (pH 6.0) at 60°C for 20 minutes. Primary antibodies (Table 1) were applied overnight at 4°C in PBS containing 0.2% Triton X-100 and 1% BSA. After washing, sections were incubated for 1 hour at RT with Alexa Fluor–conjugated secondary antibodies and DAPI (1:1000) for nuclear counterstaining. Slides were then mounted and prepared for imaging. The same protocol was used for conventional in vitro immunofluorescence. For live-cell mitochondrial labelling, MitoTracker Deep Red was used according to the manufacturer's instructions. Briefly, cells cultured on glass-bottom chamber slides (Cellvis) were washed with PBS after 24 hours of coculture and incubated with MitoTracker Deep Red (200 nM) for 40 minutes in Krebs medium at 37°C, protected from light and in the absence of CO_2. Cells were then washed with PBS and immediately imaged. For DiI and phalloidin labelling, neurons were stained prior to coculture with microglia or isolated mitochondria following the manufacturers' protocols. Briefly, cells were incubated with the respective dyes for 30 minutes at 37°C, washed three times with PBS, and subsequently subjected to coculture for 24 hours before analysis.

Table 1
List of Antibodies

Antibody	Company	Catalogue	Conc.
Mouse Anti-MAP2 (Mt-01)	Novus Biologicals	NB500-415	1:500
Phalloidin-Ifluor 647 Reagent	Abcam	ab176759	1:1000
Rabbit Anti-POMC	Phoenix Pharmaceuticals	H-029-30	1:200
Mouse Anti-AgRP	R&D Systems	AF634	1:1000
Mouse Anti-NeuN	Chemicon	MAB377	1:1000
GFAP Monoclonal Antibody (2.2b10), Alexa Fluor™ 647	Invitrogen	51-9792-82	1:500
Rabbit Anti-Tyrosine Hydroxylase	Sigma-Aldrich	AB152	1:500
DAPI	Sigma-Aldrich	D9542	1:1000
Mitotracker Deep Red FM	Thermo Fisher Scientific	M22426	200nM
Mitotracker Red CMXRos	Thermo Fisher Scientific	M7512	200nM
Dil Stain	Thermo Fisher Scientific	D282	1:1000
Donkey Anti-Rabbit IgG Alexa Fluor 594	Jackson ImmunoResearch	711-585-152	1:1000
Donkey Anti-Rabbit IgG Alexa Fluor 647	BioLegend	406414	1:500
Donkey Anti-Goat IgG (H + L) Alexa Fluor 647	Jackson ImmunoResearch	705-605-003	1:500
Donkey Anti Mouse IgG (H + L) Alexa Fluor 647	Invitrogen	A-31571	1:500
Rabbit Anti-NDUFS1 [Epr11521(B)]	Abcam	ab169540	1:1000
Rabbit Anti-UQCRC2 [Epr13051]	Abcam	ab203832	1:1000
Rabbit Anti-TOMM20	Thermo Fisher Scientific	PA5-52843	1:1000
Rabbit Anti-Phospho-STAT3 (Tyr705)	Cell Signaling Technology	9131S	1:1000
Rabbit Anti-beta-Actin (13e5)	Cell Signaling Technology	4970S	1:1000
Peroxidase (HRP) Anti-Rabbit IgG	Cell Signaling Technology	7074S	1:10.000
Peroxidase (HRP) Anti-Mouse IgG	Cell Signaling Technology	7074S	1:10.000

Antibody	Company	Catalogue	Conc.
Zombie Violet	BioLegend	423114	1:1000
CD11b BB660	BioLegend	101228	1:100
Mitosox	Thermo Fisher Scientific	M36008	5µm

Image Acquisition

All microscopy experiments were performed at the Institute of Advanced Studies on Photonics Applied to Cell Biology (INFABiC), UNICAMP, São Paulo, Brazil. High-resolution confocal images were acquired using a Zeiss LSM 880 confocal microscope equipped with an Airyscan super-resolution detector (Carl Zeiss AG, Germany). DAPI was excited using a 405 nm diode laser (5% power), while green, red, and far-red fluorophores were excited using 488 nm, 561 nm, and 633 nm lasers, respectively. Laser power and detector gain were adjusted according to staining conditions, and fluorescence signals were typically detected using photomultiplier tube (PMT) detectors. Images were acquired with a frame size of 1024 × 1024 pixels, line step of 0.5 µm, scan speed of 4 to 8, bidirectional scanning, and either 8- or 16-bit depth. For tissue sections, z-stacks spanning 10–20 µm were acquired in 8-bit mode. During automated Airyscan acquisitions, a zoom factor of 1.8 was applied, and the detector was positioned at the center of the Airyscan disk to ensure optimal signal quality. Airyscan super-resolution reconstruction was performed in ZEN software. For whole sagittal mouse brain sections, mosaic images were acquired using an inverted Zeiss Axio Observer.Z1 microscope equipped with a Yokogawa CSU-X1 spinning disk confocal unit, an iXon3 camera, and iQ3 software (Andor). Images were acquired in 16-bit mode using 488, 561, and 640 nm lasers with corresponding emission filters (525/30, 607/36, and 685/40 nm), a zoom factor of 1.0, and a 40×/1.4 NA oil-immersion objective. Z-stacks were collected at 4 µm intervals with a resolution of 512 × 512 pixels. Mosaic reconstruction was performed using the MosaicJ plugin in FIJI/ImageJ software.

Fluorescence Lifetime Imaging Microscopy

Fluorescence lifetime imaging microscopy (FLIM) based on two-photon excitation fluorescence (TPEF) was performed on Clu189 neurons using an inverted Zeiss LSM780 NLO Axio Observer confocal microscope (Carl Zeiss AG, Germany). The system was equipped with a time-correlated single-photon counting (TCSPC) module (Becker & Hickl) and a femtosecond pulsed laser (100 fs pulse duration, 80 MHz repetition rate; Chameleon Discovery Nx, Coherent Inc., USA). Cells were maintained at 37°C in a humidified atmosphere containing 5% CO_2 throughout acquisition to preserve physiological conditions. Endogenous NAD(P)H and FAD autofluorescence were simultaneously excited at 760 nm with a mean laser power of 10 mW at the objective back aperture and focused using an EC Plan-Neofluar 40×/1.3 NA oil-immersion objective. Emission signals were detected by two single-photon counting PMTs (Becker & Hickl, SPC-830) after passing through 445/45 nm (NAD(P)H) and 535/22 nm (FAD) band-pass filters. A 690 nm short-pass filter was used to block excitation light at the detector entrance. Images were acquired with a field of view of 512 × 512 pixels (212.55 × 212.55 µm), and fluorescence decay curves

were collected for 120 seconds per field. FLIM data were processed using SPCImage software (version 2.9; Becker & Hickl). A bi-exponential decay model was applied to fit fluorescence decay curves at each pixel, generating pseudocolor lifetime maps. Mean lifetime (τm), short (τ1) and long (τ2) lifetime components, and the relative amplitudes of free (a1) and protein-bound (a2) fluorophore fractions were extracted for downstream analysis.

Time-Lapse Imaging

Time-lapse imaging of primary microglia isolated from LysM-CrePhAM^{floxed} mice and microglia–neuron coculture systems was performed using a Zeiss LSM 880 confocal microscope equipped with an Airyscan detector. Cells were plated in four-well chamber slides with glass coverslips (500 µL completed DMEM/well) and maintained at 37°C in a humidified atmosphere with 5% CO_2 throughout imaging. Images were acquired using either a Plan-Apochromat 40×/1.3 NA or a Plan-Neofluar 63×/1.4 NA oil-immersion objective. For high-resolution visualization of mitochondrial morphology and subcellular structures, images were acquired with two-frame averaging, a z-step size of 0.5 µm, 16-bit depth, 1024 × 1024-pixel resolution, a zoom factor of 1.8×, and pinhole size set to 1 Airy unit (13.65 pixel/µm). For three-dimensional visualization of Dendra2-expressing cells, excitation was performed using a 488 nm laser (5% power), and z-stacks were acquired at 1 µm intervals (5–10 optical sections per acquisition). Time-lapse series were acquired for up to 24 hours, with acquisition intervals optimized for each experiment; in most cases, images were captured every 300 seconds for a total of 40 frames. Neurons and microglia were identified using brightfield imaging or fluorescent markers, including MitoTracker Deep Red, phalloidin, or DiI. Airyscan processing was applied post-acquisition to enhance spatial resolution of Dendra2-positive mitochondria and cellular interactions.

Image Analysis

All image processing and quantitative analyses were performed using FIJI/ImageJ software (NIH). For three-dimensional analyses, image stacks were pre-processed to reduce noise and enhance signal quality. Preprocessing steps included application of a Gaussian blur filter, background subtraction using the “Subtract Background” function, and thresholding to generate binary masks. Thresholded images were analyzed using the Mitochondrial Analyzer plugin[36] (version 2.0.2) to quantify mitochondrial morphology parameters in microglia. Colocalization between fluorescent signals was assessed either by visual inspection of orthogonal views or by fluorescence intensity–based colocalization analysis, as appropriate for each experiment. Quantification of TH$^+$ neuronal cell bodies and Dendra2$^+$ neurons within the VMH was performed manually using the Cell Counter plugin. TH$^+$ neuronal fiber density was quantified by measuring integrated density (IntDen) of the TH immunoreactive signal. Neuronal survival was quantified by counting DAPI$^+$ nuclei per well, which served as a proxy for total neuron number under the indicated experimental conditions. For three-dimensional representations, it was used Imaris software (Bitplane/Oxford Instruments).

Flow Cytometry Analysis

Cells were stained with Zombie Violet viability dye and with anti-CD11b–PerCP (Table 1) to identify microglial populations. Following surface staining, cells were fixed and permeabilized using Cytofix/Cytoperm solution (BD Biosciences, Cat. #554722) according to the manufacturer's instructions. Neuronal populations were identified by intracellular staining with an anti-NeuN primary antibody diluted in Perm/Wash buffer, followed by incubation with an Alexa Fluor 647–conjugated secondary antibody.

Flow cytometry was performed on a FACSymphony A5 SE cytometer (BD Biosciences) following the gating strategy: FSC/SSC → singlets → live cells → $CD11b^-$ → $NeuN^+$ neurons. A minimum of 10,000 events per sample was collected. Compensation was performed using BD compensation beads. Mitochondrial content and membrane potential were assessed using MitoTracker Deep Red (APC channel), while PhAM-derived mitochondrial fluorescence was detected in the FITC/BB515 channel. Data were analyzed using FlowJo software (BD Biosciences). For all analyses, fluorescence-minus-one (FMO) controls were included to define gating thresholds, and parameters were quantified as either mean fluorescence intensity (MFI) or percentage of positive cells, as indicated.

Assessment of Neuronal ROS Production

Reactive oxygen species (ROS) production in Clu189 neuronal cells was evaluated using complementary Amplex Red–based assays to measure total ROS and flow cytometry–based detection of mitochondrial superoxide. For Amplex Red assays, Clu189 neurons were plated at varying densities (10,000–100,000 cells per well) to assess the influence of cell number on ROS signal. Based on these preliminary analyses, a density of 25,000 cells per well was selected for all quantitative comparisons to minimize confluency- and density-dependent bias. Cells were stimulated with rotenone at the indicated concentrations and exposure times, including acute (10 or 30 minutes) and prolonged (6 or 24 hours) treatments. In selected conditions, neurons were cocultured with microglia or exposed to microglia-derived mitochondrial preparations. Amplex Red assays were performed according to the manufacturer's instructions (Thermo Fisher Scientific, Cat. #A12222). Briefly, freshly prepared reagents, including superoxide dismutase (SOD; 1 U/mL), horseradish peroxidase (0.1 U/mL), and digitonin (5 µg/mL), were prepared in Krebs buffer, with pH verified prior to measurement. Cells were washed with PBS, after which 100 µL of Krebs buffer containing Amplex Red (50 µM), SOD, peroxidase, and digitonin was added to each well. Fluorescence was measured using a plate reader at 37°C with kinetic acquisition over 1 h 30 min at 10-minute intervals (excitation 540/35 nm; emission 600/40 nm). Fluorescence signals were normalized to nuclear staining (DAPI) to account for differences in cell numbers. For flow cytometric assessment of mitochondrial ROS, Clu189 neurons were stained with MitoSOX Red (5 µM) for 10 minutes at 37°C in serum-free DMEM, followed by washing with PBS prior to acquisition.

Seahorse Metabolic Analysis

Clu189 neurons were plated at 15,000 cells per well and exposed to microglia-derived mitochondria for 24 hours. Real-time measurements of oxygen consumption rate (OCR) and extracellular acidification rate (ECAR) were measured using an XFe96 Extracellular Flux Analyzer (Agilent Seahorse Bioscience), according to the manufacturer's instructions. Each condition was analyzed in three technical replicates.

For each assay, three consecutive baseline measurements were obtained, followed by sequential injections of metabolic inhibitors or activators specific to each test. In the mitochondrial stress test, oligomycin (1 µM), FCCP (1 µM), and a combination of rotenone (100 nM) and antimycin A (1 µM) were injected sequentially (all reagents from Sigma-Aldrich). In the glycolytic stress test, glucose (25 mM), oligomycin (1.5 µM), and 2-deoxyglucose (2-DG; 50 mM) were sequentially added. Seahorse assay medium was supplemented with 10mM glucose, 1mM pyruvate, and 2mM glutamine. Metabolic parameters were calculated using Seahorse Wave software and normalized to total protein content per well to account for differences in cell number.

CRISPR-Cas9 experiments

A second-generation lentiviral system was used for CRISPR–Cas9–mediated gene perturbation. Lentiviral particles were produced using the packaging plasmid psPAX2 and the envelope plasmid pMD2.G, together with the sgRNA expression vector LentiGuide-Puro. Single-guide RNA (sgRNA) sequences complementary to the target genes were cloned into the LentiGuide-Puro backbone according to standard protocols. For virus production, HEK293T packaging cells were plated at a density of 7×10^5 cells per well in six-well plates and incubated for 18–24 hours. Cells were transfected with a mixture of the three lentiviral plasmids using polyethyleneimine (PEI). After 18–24 hours, the medium was replaced with fresh culture medium. Viral supernatants were collected at 48, 72, and 96 hours post-transfection, centrifuged at 500 × g for 5 minutes to remove cellular debris, and filtered through a 0.45-µm PES filter. Filtered viral supernatants were snap-frozen in liquid nitrogen and stored at − 80°C until use. For neuronal transduction, Clu189 neuronal cells expressing Cas9 were infected after 6 days in culture with lentiviral particles carrying sgRNAs targeting Gja1 (TCGCTGATCCACGATAGCTA), Itgb1 (GAAAATAGCAAATTGCCAGACGG), Exoc1 (GTCCGAGATAGAGTTCCTCGTGG), or Gm609 (sgRNA: AGGGTAAACGGAGATTCCAGGGG), with sgGFP used as a non-targeting control. Cells were incubated with lentivirus for 24 hours, after which viral media was replaced with fresh medium containing puromycin (1 µg/mL) for selection of sgRNA-expressing cells. Medium containing puromycin was refreshed as needed to maintain selection. For mitochondrial transfer assays, Clu189 Cas9 cells were expanded in complete DMEM without ciprofloxacin and plated at a density of 3.5×10^5 cells per well in six-well plates, in triplicate for each sgRNA condition. Cells were transduced with 200 µL of lentiviral particles per well and maintained for 48 hours. Viral media was removed, and antibiotic selection was initiated using blasticidin to maintain Cas9 expression and puromycin to select for sgRNA integration. Antibiotic concentrations were adjusted as needed to ensure effective selection. Knockout efficiency was assessed by quantitative PCR prior to coculture experiments. Neuronal uptake of microglia-derived mitochondria was subsequently evaluated by flow cytometry.

Transmission Electron Microscopy

Mitochondria were isolated from microglia as previously described, centrifuged at 12,000 g during 30 min and then, fixed in 2.5% glutaraldehyde prepared in 0.1 M sodium cacodylate buffer containing 3 mM $CaCl_2$ for 5 minutes at RT, followed by incubation on ice for 2 hours. After fixation, samples were washed three times for 2 minutes each in 0.1 M sodium cacodylate buffer containing 3 mM $CaCl_2$ and post-fixed

for 1 hour in 1% osmium tetroxide supplemented with 0.8% potassium ferrocyanide, diluted in 0.1 M sodium cacodylate buffer. Samples were then washed three times for 2 minutes each in Milli-Q water and stained en bloc overnight on ice with 2% uranyl acetate. Following staining, samples were washed three times for 2 minutes each in Milli-Q water and dehydrated through a graded ethanol series (30%, 50%, 70%, and 90% for 10 minutes each, followed by 100% ethanol three times for 10 minutes each). After dehydration, samples were incubated in a 1:1 mixture of EMbed 812 resin and 100% ethanol for 30 minutes, followed by infiltration in pure EMbed 812 resin for at least 1 hour per step (five changes). Samples were then polymerized at 60°C for 72 hours. Ultrathin sections (63 nm) were obtained using an ultramicrotome (Leica UCT) and sequentially stained with 2% uranyl acetate and Reynolds' lead citrate. Electron micrographs were acquired using a Tecnai G2 Spirit BioTWIN transmission electron microscope (FEI Company, Hillsboro, OR, USA) operated at an accelerating voltage of 80 kV.

Reverse Transcription Quantitative PCR

Total RNA was isolated from neuronal cells using TRI Reagent (Sigma-Aldrich, Cat. #T9424) according to the manufacturer's instructions. RNA concentration and purity were assessed by spectrophotometry, and for cDNA synthesis, 2 µg of total RNA was reverse-transcribed using the High-Capacity cDNA Reverse Transcription Kit (Applied Biosystems), following the manufacturer's protocol. Quantitative real-time PCR was performed using the QuantiNova® SYBR® Green PCR Kit (Qiagen, Cat. #208056). Each reaction contained 60 ng of cDNA template and 200 nM of gene-specific forward and reverse primers (Table 2). Amplification was carried out on a CFX384 Touch Real-Time PCR Detection System (Bio-Rad) under standard cycling conditions recommended by the manufacturer. All samples were run in technical triplicates, and no-template controls were included to assess potential contamination. Gene expression levels were quantified using CFX Manager Software v2.0 (Bio-Rad) and calculated using the 2^−ΔΔCt method. Expression values were normalized to mouse 18S rRNA as the reference gene and expressed relative to the appropriate experimental control group (unstimulated cells). For AgRP expression analysis, neurons were incubated for 24 hours with microglia-derived mitochondria in glucose-free DMEM. Cells were then washed with PBS and harvested for RNA isolation. For all other target genes, neurons were cultured in high-glucose DMEM prior to RNA extraction.

Table 2
List of Primers

Primers	F	R
Tnfα	5'-AGATAGCAAATCGGCTGACG-3'	5'-ACGGCATGGATCTCAAAGAC-3'
Agrp	5'-CTTTGGCGGAGGTGCTAGAT-3'	5'-AGGACTCGTGCAGCCTTACAC-3'
Pomc	5'-CGAGATTCTGCTACAGTCGCT-3'	5'-GACGTACTTCCGGGGGTTTT-3'
Exoc1	5'-TGCCATCAAAGAGAGCCCTG-3'	5'-CCAGGTGCAGGAGATGAAGG-3'
Gja1 (cnx43)	5'-TCCTTTGACTTCAGCCTCCA-3'	5'-CCATGTCTGGGCACCTCT-3'
Gm609/isec1	5'-CTTTCAGTTCAGCTAGGAAACAC-3'	5'-CTTACCTTTTCTTTTGGAAATAAAT-3'
Itgb1 1	5'- GTCGTGTGTGTGAGTGCAAC-3'	5'- GCTGGGGTAATTTGTCCCGA-3'
Itgb1 2	5"-GCAGGGCCAAATTGTGGGTGGT-3"	5"-GGCCGGAGCTTCTCTGCCAT-3"

Western Blot Analysis

Cells were lysed in RIPA buffer supplemented with protease and phosphatase inhibitor cocktails (Thermo Scientific, Cat. #78440 and #78420). Protein concentration was determined using the Pierce™ BCA Protein Assay Kit (Thermo Scientific, Cat. #23225), according to the manufacturer's instructions. For isolated mitochondria obtained from microglia or culture supernatants, samples were prepared using the mitochondrial extraction buffer provided in the cell fractionation kit (Abcam, Cat. #ab65320). Equal amounts of protein (20 µg per lane) were separated on 10% SDS–PAGE gels and electrophoresed for approximately 2 hours, followed by transfer onto PVDF membranes (Immobilon-P, Millipore, Cat. #IPVH00010) for 1.5 hours. Membranes were blocked with 5% non-fat dry milk prepared in Tris-buffered saline containing 0.1% Tween-20 (TBS-T) for 1 hour at RT. Membranes were then washed three times with TBS-T and incubated overnight at 4°C with primary antibodies (Table 1) diluted in the blocking buffer. After washing, membranes were incubated for 1 hour at RT with horseradish peroxidase (HRP)–conjugated secondary antibodies. Protein bands were visualized using the Pierce™ Fast Western Blot Kit (Thermo Scientific, Cat. #35050) in combination with SuperSignal™ West Femto Maximum Sensitivity Substrate (Thermo Scientific, Cat. #34095). Chemiluminescent signals were detected using a ChemiDoc™ Imaging System (Bio-Rad). Band intensities were quantified using ImageJ software after normalization to β-actin.

Statistical Analysis

Data are presented as mean ± SD or SEM, as indicated. All datasets were tested for normality using the Shapiro-Wilk test prior to parametric analysis, and outliers were identified and removed using the Grubbs' test (alpha = 0.05). Comparisons between two groups were performed using unpaired two-tailed Student's *t* tests, and comparisons among multiple groups were analyzed using one-way ANOVA with

Bonferroni post hoc correction. Statistical analyses were conducted using GraphPad Prism version 6.0 (GraphPad Software). Statistical significance was defined as $p < 0.05$.

Declarations

Competing Interests

The authors declare no competing interests.

Acknowledgements

The authors thank INFABIC (Imaging Facility of the University of Campinas) for technical assistance and access to microscopy infrastructure.

Funding Declaration

This work was supported by the São Paulo Research Foundation (FAPESP: grant no. 2020/16030-0, 2023/17089-6, 2022/04576-3, 2019/25973-8 and fellowship no. 2020/08744-2 and2022/05429-4); the Brazilian National Council for Scientific and Technological Development – CNPq (Grant number 434538/2018-3, 407429/2025-5); and the Coordenação de Aperfeiçoamento de Pessoal de Nível Superior – Brazil (CAPES) (Finance Code 001.

Authors Contribution

M.K.S.C.A. conceived the study, performed experiments, analyzed the data and wrote the original draft of the manuscript. L.F.L.S., G.C., W.S.S.G., R.D.R., G.A.S.N., A.T.P.C., W.L.G.C., M.B. and F.B.S.T. contributed to experimental investigations. C.B. managed resources, including laboratory organization and procurement. A.T.P.C. and M.O.B. assisted with image acquisition protocols. H.C. provided technical support for image acquisition at INFABIC. L.A.V. provided cell lines and contributed to scientific discussion of in vitro methodologies. P.M.M.M.V. conceived and supervised the study, reviewed and edited the manuscript, funding acquisition. All authors read and approved the final version of the manuscript.

References

1. Sarkar S, et al. Mitochondrial impairment in microglia amplifies NLRP3 inflammasome proinflammatory signaling in cell culture and animal models of Parkinson’s disease. npj Parkinson’s Disease. 2017;3:30.
2. Li Y, Xia X, Wang Y, Zheng JC. Mitochondrial dysfunction in microglia: a novel perspective for pathogenesis of Alzheimer’s disease. J Neuroinflammation. 2022;19:248.
3. Wang Y et al. The role of mitochondrial dynamics in disease. *MedComm* 4, e462 (2023).

4. Scheiblich H, et al. Microglia rescue neurons from aggregate-induced neuronal dysfunction and death through tunneling nanotubes. Neuron. 2024;112:3106–e31258.
5. Joshi AU, et al. Fragmented mitochondria released from microglia trigger A1 astrocytic response and propagate inflammatory neurodegeneration. Nat Neurosci. 2019;22:1635–48.
6. Liu D, et al. Intercellular mitochondrial transfer as a means of tissue revitalization. Signal Transduct Target Ther. 2021;6:65.
7. Orihuela R, McPherson CA, Harry GJ. Microglial M1/M2 polarization and metabolic states. Br J Pharmacol. 2016;173:649–65.
8. Zhong G, et al. Autologous transplantation of mitochondria/rAAV IGF-I platforms in human osteoarthritic articular chondrocytes to treat osteoarthritis. Mol Ther. 2025;33:2900–12.
9. Pham AH, McCaffery JM, Chan DC. Mouse lines with photo-activatable mitochondria (PhAM) to study mitochondrial dynamics. Genesis. 2012;50:833–43.
10. Belsham DD, et al. Ciliary neurotrophic factor recruitment of glucagon-like peptide-1 mediates neurogenesis, allowing immortalization of adult murine hypothalamic neurons. FASEB J. 2009;23:4256–65.
11. Li N, et al. Mitochondrial complex I inhibitor rotenone induces apoptosis through enhancing mitochondrial reactive oxygen species production. J Biol Chem. 2003;278:8516–25.
12. Xiong N, et al. Mitochondrial complex I inhibitor rotenone-induced toxicity and its potential mechanisms in Parkinson's disease models. Crit Rev Toxicol. 2012;42:613–32.
13. Dash C, Saha T, Sengupta S, Jang HL. Inhibition of Tunneling Nanotubes between Cancer Cell and the Endothelium Alters the Metastatic Phenotype. Int J Mol Sci. 2021;22:6161.
14. van der Vlist M, et al. Macrophages transfer mitochondria to sensory neurons to resolve inflammatory pain. Neuron. 2022;110:613–e6269.
15. Werner E, Werb Z. Integrins engage mitochondrial function for signal transduction by a mechanism dependent on Rho GTPases. J Cell Biol. 2002;158:357–68.
16. Nair S, et al. Lipopolysaccharide-induced alteration of mitochondrial morphology induces a metabolic shift in microglia modulating the inflammatory response in vitro and in vivo. Glia. 2019;67:1047–61.
17. Du Y, Brennan FH, Popovich PG, Zhou M. Microglia maintain the normal structure and function of the hippocampal astrocyte network. Glia. 2022;70:1359–79.
18. Abudara V, et al. Activated microglia impairs neuroglial interaction by opening Cx43 hemichannels in hippocampal astrocytes. Glia. 2015;63:795–811.
19. Yin X, et al. Roles of astrocytic connexin-43, hemichannels, and gap junctions in oxygen-glucose deprivation/reperfusion injury induced neuroinflammation and the possible regulatory mechanisms of salvianolic acid B and carbenoxolone. J Neuroinflammation. 2018;15:97.
20. Batsuuri K, Toychiev AH, Viswanathan S, Wohl SG, Srinivas M. Targeting Connexin 43 in Retinal Astrocytes Promotes Neuronal Survival in Glaucomatous Injury. Glia. 2025;73:1398–419.

21. Iorio R, Petricca S, Di Emidio G, Falone S, Tatone C. Mitochondrial Extracellular Vesicles (mitoEVs): Emerging mediators of cell-to-cell communication in health, aging and age-related diseases. Ageing Res Rev. 2024;101:102522.
22. Paliwal S, Chaudhuri R, Agrawal A, Mohanty S. Regenerative abilities of mesenchymal stem cells through mitochondrial transfer. J Biomed Sci. 2018;25:31.
23. Shanmughapriya S, Langford D, Natarajaseenivasan K. Inter and Intracellular mitochondrial trafficking in health and disease. Ageing Res Rev. 2020;62:101128.
24. Zampieri LX, Silva-Almeida C, Rondeau JD, Sonveaux P. Mitochondrial Transfer in Cancer: A Comprehensive Review. Int J Mol Sci. 2021;22:3245.
25. Li X, et al. Accumulation of Damaging Lipids in the Arf1-Ablated Neurons Promotes Neurodegeneration through Releasing mtDNA and Activating Inflammatory Pathways in Microglia. Adv Sci. 2025;12:2414260.
26. Todkar K, et al. Selective packaging of mitochondrial proteins into extracellular vesicles prevents the release of mitochondrial DAMPs. Nat Commun. 2021;12:1971.
27. Ikeda G, et al. Mitochondria-Rich Extracellular Vesicles From Autologous Stem Cell–Derived Cardiomyocytes Restore Energetics of Ischemic Myocardium. JACC. 2021;77:1073–88.
28. Lu Y, et al. Protective role of mitophagy on microglia-mediated neuroinflammatory injury through mtDNA-STING signaling in manganese-induced parkinsonism. J Neuroinflammation. 2025;22:55.
29. Zhu J, et al. ATF5 Attenuates the Secretion of Pro-Inflammatory Cytokines in Activated Microglia. Int J Mol Sci. 2023;24:3322.
30. Kim J-H, Lee Y, Suh GY, Lee Y-S. Mul1 suppresses Nlrp3 inflammasome activation through ubiquitination and degradation of Asc. bioRxiv. 2019;830380. 10.1101/830380.
31. Moraes-Vieira PM, et al. Antigen Presentation and T-Cell Activation Are Critical for RBP4-Induced Insulin Resistance. Diabetes. 2016;65:1317–27.
32. Cannon JR, et al. A highly reproducible rotenone model of Parkinson's disease. Neurobiol Dis. 2009;34:279–90.
33. Fleming SM, et al. Early and Progressive Sensorimotor Anomalies in Mice Overexpressing Wild-Type Human α-Synuclein. J Neurosci. 2004;24:9434–40.
34. *Paxinos and Franklin's the Mouse Brain in Stereotaxic Coordinates*. (2022).
35. Maness LM, Kastin AJ, Farrell CL, Banks WA. Fate of leptin after intracerebroventricular injection into the mouse brain. Endocrinology. 1998;139:4556–62.
36. Chaudhry A, Shi R, Luciani DS. A pipeline for multidimensional confocal analysis of mitochondrial morphology, function, and dynamics in pancreatic β-cells. Am J Physiol Endocrinol Metab. 2020;318:E87–101.

Figures

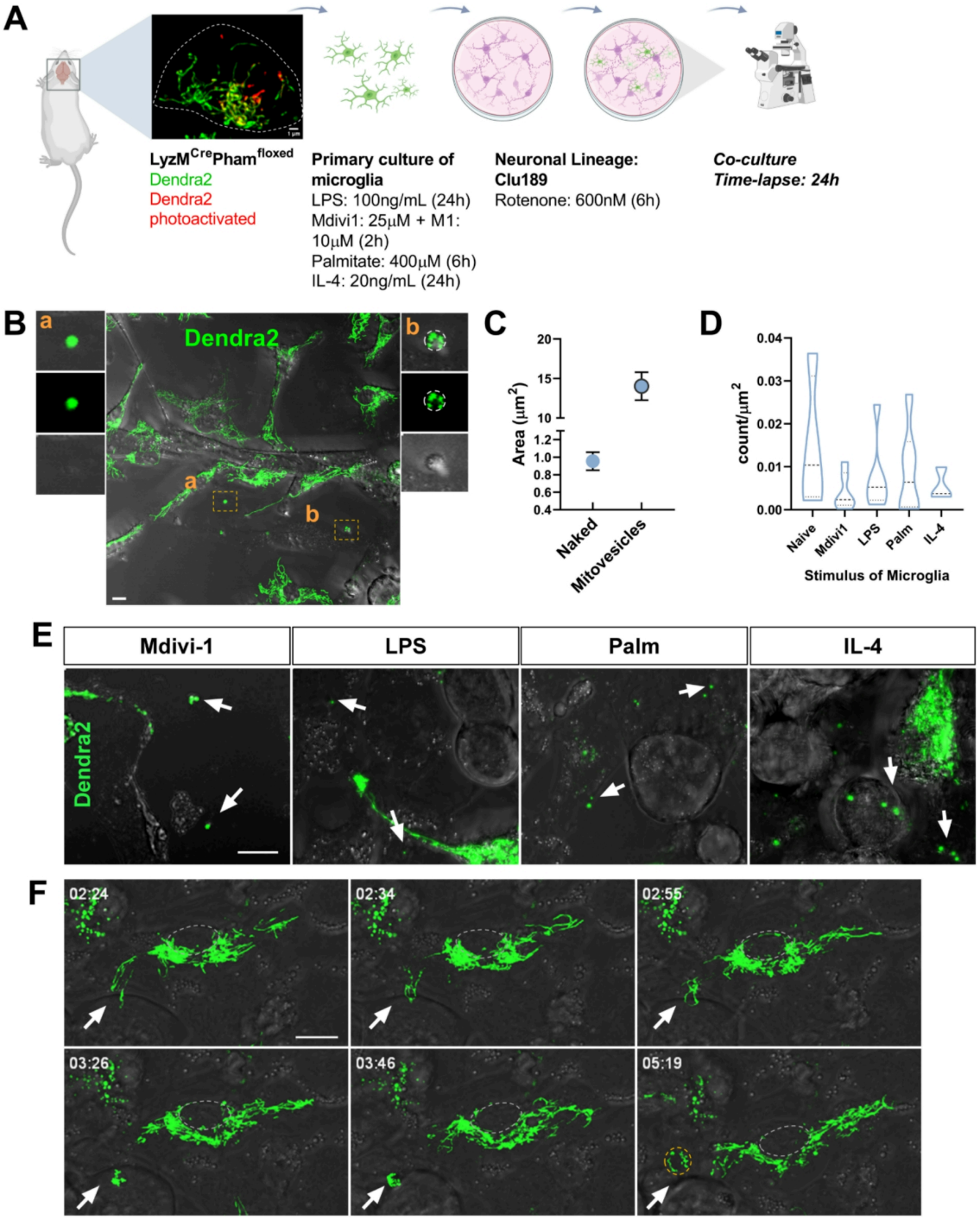


Figure 1

Microglia release mitochondria into the extracellular space in vitro.

(A) Schematic representation of the experimental design. Primary microglia were isolated from *LyzM-CrePham*^{floxed} mice expressing Dendra2-labeled mitochondria and stimulated as indicated prior to co-culture with the neuronal cell line Clu189. Extracellular mitochondrial release was analyzed by live imaging.

(B) Representative image of co-culture between Clu189 cells (brightfield) and primary microglia (Dendra2^{+}, green). Extracellular Dendra2^{+} mitochondria were detected in two forms: naked mitochondria (inset a) and mitochondria enclosed within vesicular structures (mitovesicles; inset b).

(C) Quantification of the area of microglia-derived extracellular mitochondria, comparing naked mitochondria and mitovesicles. N = 12-15 images.

(D) Quantification of extracellular mitochondria released by microglia following stimulation with the indicated treatments prior to co-culture. N = 6 images.

(E) Representative images of microglia co-cultured with Clu189 cells, showing extracellular mitochondria released after microglia were pre-treated with the indicated stimuli. Arrows indicate extracellular mitochondria.

(F) Time-lapse sequence showing mitovesicle release from a microglial cell after approximately 2 h of co-culture with Clu189 cells. Dashed outline indicates the released mitovesicle.

Data are expressed as mean ± SEM.

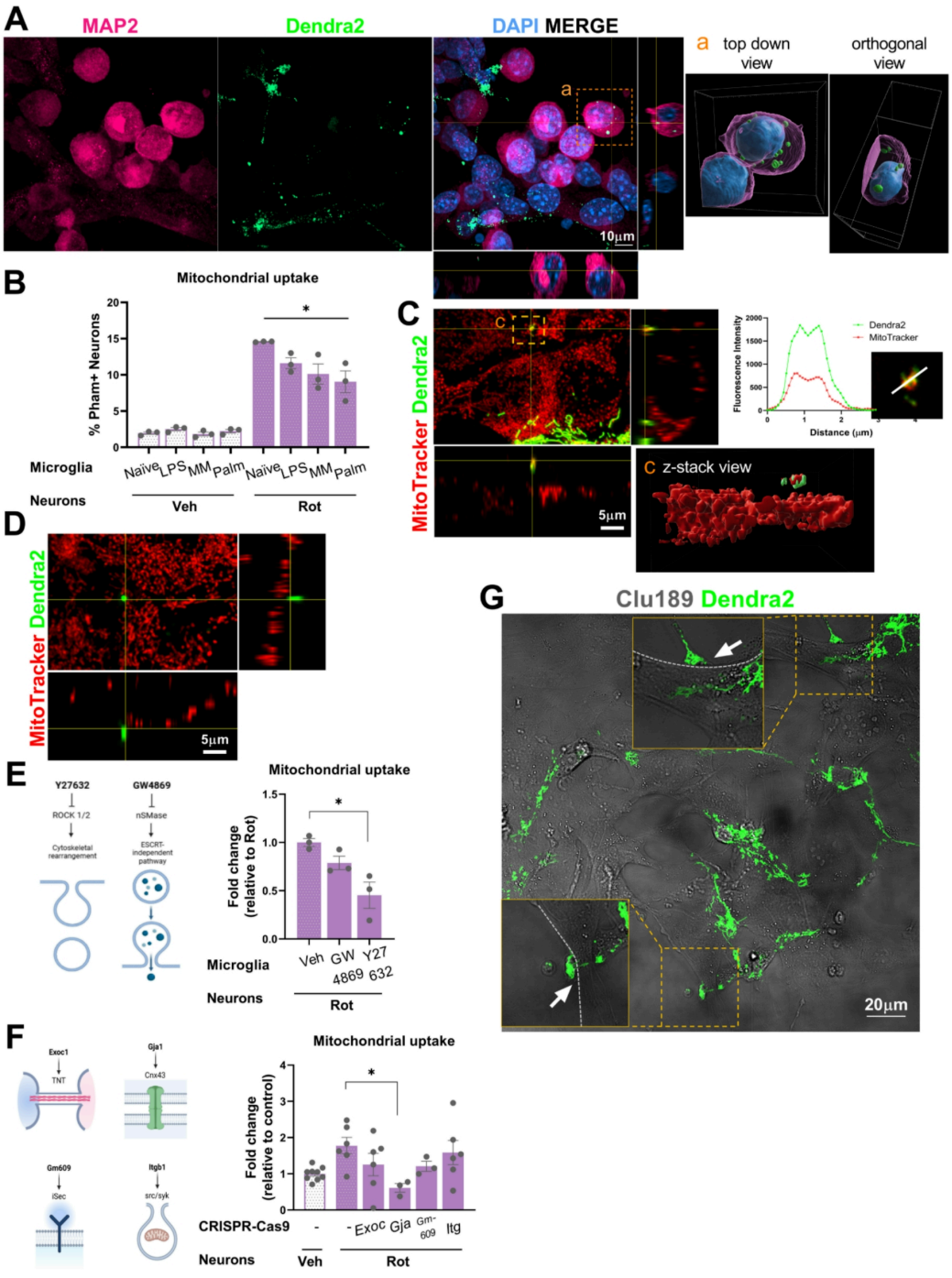


Figure 2

Neurons internalize microglia-derived mitochondria

(A) Representative confocal image of co-culture between primary microglia expressing Dendra2-labeled mitochondria (green) and Clu189 neurons ($MAP2^+$, magenta; nuclei stained with DAPI, blue). Inset (a) shows a neuronal soma containing internalized $Dendra2^+$ mitochondria derived from microglia.

Orthogonal (x–z and y–z) views confirm intracellular localization. Three-dimensional (3D) reconstructions of the inset region further demonstrate mitochondrial internalization within neurons.

(B) Quantification of Dendra2^{+} neurons by flow cytometry following co-culture. Neurons were treated with vehicle (Veh) or rotenone (Rot) and microglia were pre-treated with the indicated stimuli, before co-culture. Data represent the percentage of Pham^{+} neurons.

(C) Representative image showing co-localization between microglia-derived Dendra2^{+} mitochondria (green) and MitoTracker Deep Red (red). Line-scan fluorescence intensity analysis (white line) demonstrates signal overlap between channels. The same mitochondrion is shown in 3D (z-stack reconstruction, inset c), confirming co-localization.

(D) Representative image showing naked mitochondria that display minimal or no co-localization with MitoTracker Deep Red.

(E) Schematic illustration of the inhibitory pathways targeted by Y-27632 (ROCK1/2 inhibitor) and GW4869 (neutral sphingomyelinase inhibitor), together with quantification of Dendra2^{+} neurons by flow cytometry. Neurons were treated with rotenone and co-cultured with microglia pre-treated with the indicated inhibitors. Data are presented as fold change relative to rotenone-treated controls.

(F) CRISPR-Cas9-mediated gene knockdown in Clu189 neurons targeting candidate genes involved in mitochondrial transfer. Following gene editing, neurons were treated with rotenone and co-cultured with microglia. Mitochondrial uptake was quantified by flow cytometry and expressed as fold change relative to control.

(G) Representative image of co-culture showing mitochondrial-enriched microglial processes (“hubs”) in close contact with Clu189 neurons. Insets (arrows) highlight contacts sites. Dashed lines indicate cell boundaries.

Statistical analysis: Data are expressed as mean ± SEM. One-way ANOVA followed by Tukey’s post hoc test for multiple comparisons, or unpaired t-test for two-group comparisons; *$p < 0.05$.

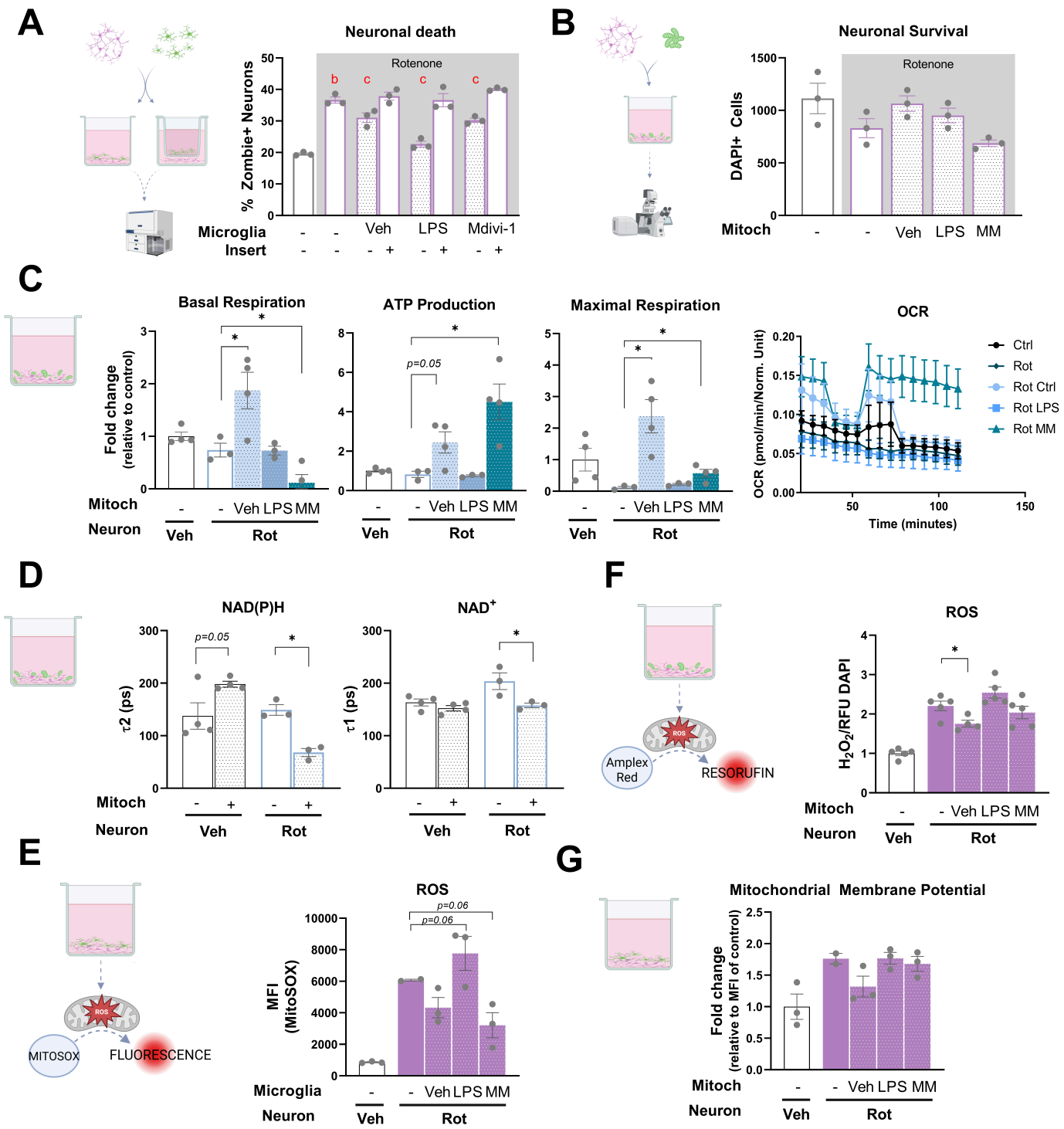


Figure 3

Microglia-derived mitochondria rescue neurons from rotenone-induced damage.

(A) Quantification of Zombie^{+} Clu189 neurons by flow cytometry following rotenone treatment and co-culture with microglia pre-treated with the indicated stimuli. In parallel experiments, microglia were

cultured in 1-μm transwell inserts to prevent direct contact and mitochondrial transfer to Clu189 neurons.

(B) Quantification of $DAPI^+$ nuclei of Clu189 neurons after 24 h treatment with mitochondria isolated from microglia previously stimulated as indicated. The first bar represents untreated control neurons; subsequent groups were treated with rotenone prior to mitochondrial supplementation.

(C) Seahorse mitochondrial stress test analysis of OCR in Clu189 neurons treated with rotenone and supplemented with mitochondria isolated from microglia exposed to the indicated stimuli. Data were normalized to neuronal protein content and expressed as fold change relative to vehicle-treated Clu189 neurons not receiving mitochondria.

(D) Fluorescence lifetime imaging microscopy (FLIM) analysis of NAD^+ and NAD(P)H lifetimes in Clu189 neurons treated with vehicle or rotenone, followed by supplementation with mitochondria isolated from naïve microglia.

(E) Flow cytometry analysis of mitochondrial reactive oxygen species (ROS) in Clu189 neurons using MitoSOX mean fluorescence intensity (MFI). Neurons were treated with rotenone and co-cultured with microglia previously stimulated with the indicated drugs.

(F) Amplex Red assay measuring H_2O_2-derived resorufin fluorescence in Clu189 neurons after treatment with microglia-derived mitochondria. Results were normalized to $DAPI^+$ neuronal fluorescence. Microglia were pre-treated with the indicated stimuli prior to mitochondrial isolation. Microglia-to-neuron ratio: 1:1.

(G) Flow cytometry analysis of mitochondrial membrane potential in Clu189 neurons using MitoTracker Deep Red MFI. Neurons were treated with rotenone and subsequently supplemented with mitochondria isolated from microglia pre-treated as indicated. Results are expressed as fold change relative to control (vehicle-treated Clu189 neurons not receiving mitochondria).

Statistical analysis: Data are expressed as mean ± SEM. One-way ANOVA followed by Tukey's post hoc test for multiple comparisons, or unpaired t-test for two-group comparisons; $*p < 0.05$.

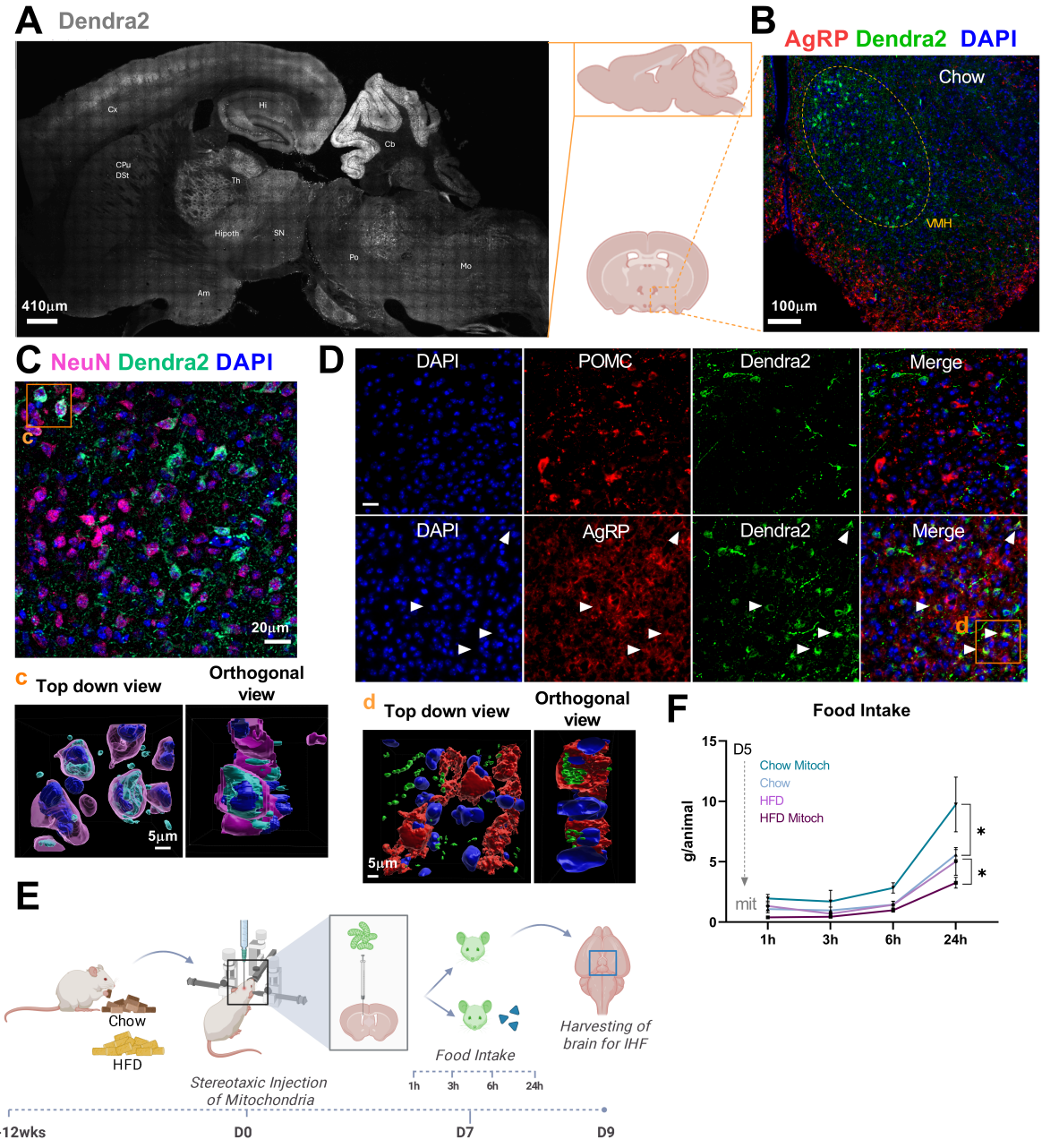


Figure 4

Microglia-to-neuron mitochondrial transfer occurs in vivo.

(A) Mosaic microscope image of a sagittal brain section from LyzM-CrePham^{floxed} mice showing Dendra2^{+} mitochondria (grey) within microglia and distributed in the extracellular space across multiple brain regions. Abbreviations: Cx, cortex; Hi, hippocampus; Cb, cerebellum; CPu, caudate-putamen; Dst, dorsal striatum; Th, thalamus; Hypoth, hypothalamus; SN, substantia nigra; AM, amygdala; PO, pons; MO, medulla oblongata.

(B) High-magnification image of the hypothalamus from a chow-fed mouse showing AgRP^{+} neurons (red), Dendra2^{+} mitochondria (green), and nuclei (DAPI, blue). The ventromedial hypothalamus (VMH) is

outlined (dashed line). Dendra2$^+$ mitochondrial signal is detected within neurons in this region.

(C) Higher magnification of the VMH showing NeuN$^+$ neurons (magenta) containing internalized Dendra2$^+$ mitochondria (green) derived from microglia. 3D reconstruction (inset c) with top-down and orthogonal views confirms intracellular localization within neuronal somata.

(D) Images of arcuate nucleus neurons stained for POMC (upper panels) or AgRP (lower panels). Dendra2$^+$ mitochondria (green) are detected within AgRP$^+$ neurons (arrowheads), whereas limited signal is observed in POMC$^+$ neurons. 3D reconstruction of the highlighted AgRP$^+$ neurons (inset d) confirms intracellular mitochondrial localization.

(E) Experimental design for stereotaxic injection of isolated mitochondria. Mice were maintained on chow or high-fat diet (HFD) for 12 weeks. Purified mitochondria were stereotaxically i.c.v injected. After 7 days of post-surgical recovery, food intake was measured at 1 h, 3 h, 6 h, and 24 h after 7 days following mitochondrial injection.

Statistical analysis: Two-way ANOVA followed by Tukey's post hoc test, or unpaired t-test for unpaired two-group comparisons. Data are presented as mean ± SEM; *$p < 0.05$.

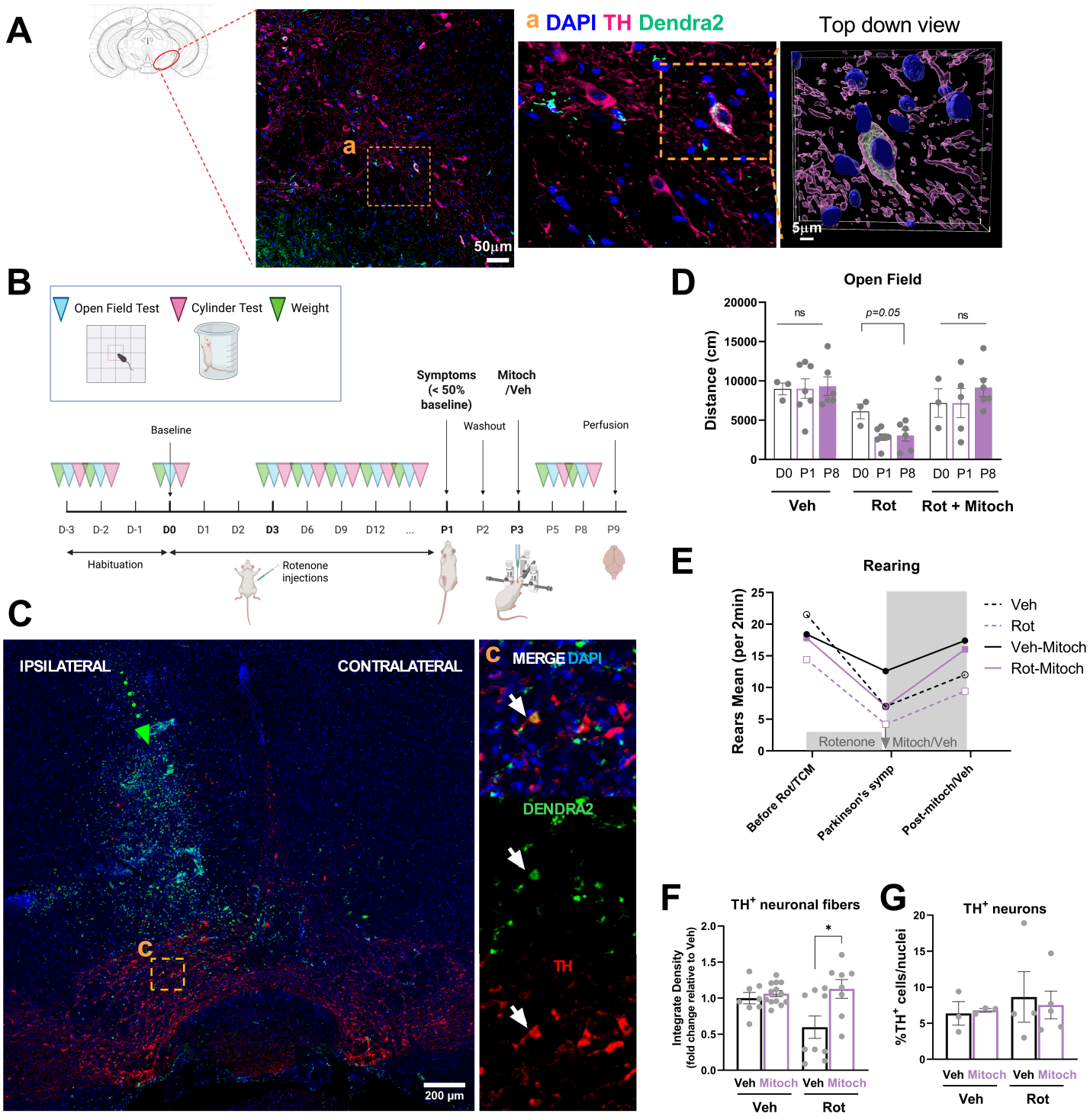


Figure 5

Dopaminergic neurons internalize microglia-derived mitochondria in vivo and mitochondrial supplementation improves motor deficits in a rotenone model.

(A) Representative confocal image of the substantia nigra pars compacta (SNpc) from LyzM-CrePham^{floxed} mice showing tyrosine hydroxylase–positive (TH^{+}) dopaminergic neurons (magenta), Dendra2^{+} microglia-derived mitochondria (green), and nuclei (DAPI, blue). Inset (a) shows a higher

magnification of the highlighted region, and 3D reconstruction confirms intracellular localization of Dendra2^{+} mitochondria within TH^{+} neurons.

(B) Experimental design of the Parkinsonian model induced by repeated intraperitoneal rotenone injections (3mg/mL). Behavioral tests (open field, cylinder/rearing test) and body weight monitoring were performed during treatment. Mice exhibiting ≥50% reduction in locomotor activity were selected for stereotaxic injection of purified mitochondria into the SNpc. A 24-h washout period was allowed between the final rotenone injection and mitochondrial administration. Behavioral assessments were repeated post-injection, followed by transcardial perfusion and brain collection for histological analysis. N = 3-6 mice.

(C) Coronal brain section showing the site of stereotaxic mitochondrial injection (30 µg mitochondrial protein) into the SNpc (green arrow) in the ipsilateral hemisphere. The contralateral hemisphere displays minimal Dendra2^{+} signal outside microglia. Inset (c) shows TH^{+} neurons containing internalized Dendra2^{+} mitochondria in the SNpc.

(D) Open field test quantification showing total distance traveled before (D0), during rotenone treatment (P1) and after (P8) mitochondrial or vehicle injection in control (Veh), rotenone-treated (Rot), and rotenone plus mitochondrial supplementation (Rot + Mitoch) groups.

(E) Rearing behavior (mean rears per 2 min) assessed before rotenone treatment (D0), during symptom manifestation (P1), and after intracerebral injection of mitochondria or vehicle (P8).

(F) Quantification of TH^{+} dopaminergic fiber integrated density (IntDen) relative to vehicle in rotenone-treated mice receiving vehicle or mitochondrial supplementation. Fibers were quantified in the striatal projection area. Images, mice: N = 3-6 mice.

(G) Quantification of TH^{+} neuronal cell bodies in the SNpc following rotenone treatment and mitochondrial supplementation. N = 3-6 mice.

Statistical analysis: Two-way ANOVA followed by Tukey's post hoc test for multiple comparisons, or unpaired t-test for unpaired two-group comparisons. Data are presented as mean ± SEM; *$p < 0.05$.

Supplementary Files

This is a list of supplementary files associated with this preprint. Click to download.

- SupplementaryMaterial.docx